AIP | Journal of Applied Physics

Plasma column and nano-powder generation from solid titanium by localized microwaves in air

Simona Popescu, Eli Jerby, Yehuda Meir, Zahava Barkay, Dana Ashkenazi, J. Brian A. Mitchell, Jean-Luc Le Garrec, and Theyencheri Narayanan

Citation: Journal of Applied Physics **118**, 023302 (2015); doi: 10.1063/1.4926491
View online: http://dx.doi.org/10.1063/1.4926491
View Table of Contents: http://scitation.aip.org/content/aip/journal/jap/118/2?ver=pdfcov
Published by the AIP Publishing

Plasma column and nano-powder generation from solid titanium by localized microwaves in air

Simona Popescu,[1] Eli Jerby,[1,a)] Yehuda Meir,[1] Zahava Barkay,[2] Dana Ashkenazi,[1] J. Brian A. Mitchell,[3] Jean-Luc Le Garrec,[3] and Theyencheri Narayanan[4]
[1]*Faculty of Engineering, Tel Aviv University, Ramat Aviv 6997801, Israel*
[2]*Wolfson Applied Materials Research Center, Tel Aviv Univ., Ramat Aviv 6997801, Israel*
[3]*IPR., U.M.R. No. 6251 du C.N.R.S., Université de Rennes I, 35042 Rennes, France*
[4]*European Synchrotron Radiation Facility, 38043 Grenoble, France*

(Received 2 May 2015; accepted 28 June 2015; published online 8 July 2015)

This paper studies the effect of a plasma column ejected from solid titanium by localized microwaves in an ambient air atmosphere. Nanoparticles of titanium dioxide (titania) are found to be directly synthesized in this plasma column maintained by the microwave energy in the cavity. The process is initiated by a hotspot induced by localized microwaves, which melts the titanium substrate locally. The molten hotspot emits ionized titanium vapors continuously into the stable plasma column, which may last for more than a minute duration. The characterization of the dusty plasma obtained is performed *in-situ* by small-angle X-ray scattering (SAXS), optical spectroscopy, and microwave reflection analyses. The deposited titania nanoparticles are structurally and morphologically analyzed by *ex-situ* optical and scanning-electron microscope observations, and also by X-ray diffraction. Using the Boltzmann plot method combined with the SAXS results, the electron temperature and density in the dusty plasma are estimated as $\sim$0.4 eV and $\sim 10^{19}\,m^{-3}$, respectively. The analysis of the plasma product reveals nanoparticles of titania in crystalline phases of anatase, brookite, and rutile. These are spatially arranged in various spherical, cubic, lamellar, and network forms. Several applications are considered for this process of titania nano-powder production.
 [http://dx.doi.org/10.1063/1.4926491]

I. INTRODUCTION

Titanium dioxide (titania) in its various forms[1] is widely used, for instance, in applications related to air cleaning,[2–4] water purification,[5–8] photo–catalysts,[9–14] semiconductors,[15,16] solar energy conversion,[17,18] paints, pigments,[19,20] food coloring, and sunscreens.[21–23] Titania has three main types of crystalline polymorphs, namely, rutile, anatase, and brookite. While they all have the same chemical formula (TiO_2), rutile and anatase have a tetragonal primitive unit cell, and brookite is orthorhombic.[24–26] The brookite and anatase phases are metastable and convert easily to rutile upon heating at temperatures in the range of 550–750 °C.[27–30] Thermodynamically, the transformation of the metastable anatase and brookite to rutile is irreversible. It is the rutile phase, thus, which is the most stable (polymorph) form of titania and hence the most common natural titanium oxide. While the rutile phase is used in most of the applications mentioned above, it is the anatase phase which is active in photo-catalysis.

Titania is synthesized by various techniques, such as spark plasma sintering,[31,32] pyrolytic processes,[33] microwave plasma torch,[34,35] cathodic arc deposition,[36] thermal plasma,[37] arc discharge method,[38] hydrothermal processes,[39] and by other chemical methods.[40,41] The synthesis temperature has a significant role in the preparation of each phase of the TiO_2 particles. Thus, the rutile phase is obtained at temperatures higher than $\sim$600 °C,[42] whereas the anatase and brookite phases are obtained at lower temperatures.

This paper presents the synthesis of titania nanoparticles in a transition mixed form of the brookite-anatase-rutile phases obtained by a microwave plasma-column technique.[43] The morphology of the titania powder produced is studied using scanning electron microscopy (SEM) and its crystallinity is characterized by X-ray diffraction (XRD). The dusty plasma obtained is analyzed *in-situ* by small-angle X-ray scattering (SAXS), optical spectroscopy, and microwave scattering. Potential applications are discussed for this technique of titania nano-powder production directly from solid titanium in air atmosphere.

II. EXPERIMENTAL SETUP

The experimental setup shown in Fig. 1 consists of a microwave cavity made of a rectangular waveguide (96 $\times$ 46 mm^2 inner cross-section). The metallic-vane windows enable a direct view of the plasma column (as in Ref. 43) with no microwave leaks. The microwave cavity is energized by a 2.45-GHz magnetron fed by a switched-mode power supply which provides an adjustable input microwave power up to $\sim$1 kW.

The titanium source plate ($\sim$20 $\times$ 10 $\times$ 1 mm^3) is positioned vertically in the cavity, as illustrated in Fig. 1. The plasma column is ejected from a hotspot created on its upper edge toward the copper collector plate (horizontally installed

a)Author to whom correspondence should be addressed. Electronic mail: jerby@eng.tau.ac.il.

TABLE I. Physical parameters of the analyzed titanium plasma-column.

Parameter	Symbol	Value	Source
Plasma column mean diameter	d_{PC}	15 mm	Observation
Effective dissipation factor	ε''_r	~300	Measurement
Average dust particle radius	r_d	~20 nm	SAXS analysis
Dust grain density	n_d	$\sim 3.8 \times 10^{17} m^{-3}$	SAXS analysis
Dust collision length factor	l_d	~2 mm	Equation (6)
Dust charging frequency	υ_{ch}	$<10^9\ s^{-1}$	Reference 55
Dust charging factor	η_{ed}	$1.3 \times 10^{14}\ F/m^2 s^2$	Equation (6)
Neutrals density	N_n	$10^{24}\ m^{-3}$	Reference 55
Neutrals cross-section	σ_n	$4.4 \times 10^{-20}\ m^2$	Reference 55
Electron collision frequency	υ	$\sim 10^{10}\ s^{-1}$	Reference 55
Electron temperature	T_e	~0.4 eV	Boltzmann plot
Electron thermal velocity	V_{Te}	$\sim 3 \times 10^5$ m/s	Reference 55
Electron density	n_e	$\sim 10^{19}\ m^{-3}$	Equation (7)

on the ceiling of the cavity). Optionally, a movable inner electrode (also made of titanium) is inserted via a hole in the ceiling, either vertically through the collector or in a 50° inclination angle as shown in Fig. 1 (thus the collector plate is uniform in the deposited area). The electrode expedites the excitation of a hotspot when brought into contact with the upper edge of the titanium source plate. In experiments done with the inclined electrode, the typical deposition time is 40–60 s (compared to ~2 min with the vertical electrode[43]) and better control is achieved over the uniformity of the deposit (which allows more homogeneous layers of titania nano-powder to be formed on the collector substrate). Setting specific time depositions (e.g., 40 or 60 s) enables the thickness of the deposited layers to be varied.

Structural and morphological analyses of the titania nanoparticles obtained from the titanium plasma columns were performed *in-situ* by SAXS, optical spectroscopy, and microwave reflectometry, and *ex-situ* using SEM and XRD analyses. The SAXS measurements (at the European Synchrotron Radiation Facility, ESRF) involved taking scattering images at a rate of 5 frames/s with the detector located at a distance of 10 m inside an evacuated flight tube. The SEM morphological imaging was performed using a Quanta 200FEG environmental SEM (ESEM). The titanium oxide content was verified using INCA software with an Oxford energy-dispersive spectrometer (EDS) with a liquid nitrogen cooled Li (Ni) detector. The optical spectral emission was captured by an optical spectrometer (Avaspec-3648) with 0.3-nm resolution in the range of 400–1000 nm (calibrated by an AvaLight Deuterium-Halogen light source DH-BAL-CAL UV/VIS).

III. EXPERIMENTAL RESULTS

A. *In-situ* observations

The plasma ejected from the titanium source is visually observed in various shapes, which may appear at different stages and operating conditions. Figures 2(a)–2(d) show images captured in various experimental runs and in different periods after ignition. The intense plasma-column mode shown in Fig. 2(b) appears to be the most common and stable mode and is therefore the main interest of this study. However, less intense plasma in the shape of a candle flame (Fig. 2(a)) tends to appear at the beginning of the process, and under reduced microwave input power. Another form, that of a detached fireball[44] shown in Fig. 2(c), may evolve at higher input power if the gap between the source plate and the ceiling is sufficiently large.

The fireball mode is less stable than the plasma column, since the fireball tends to move away and disappears in a sub-second timescale. Both modes may coexist stably though, as the fireball could be accompanied by a plasma column (or by a candle-like flame) ejected from the hotspot, as seen in Fig. 2(d). It is noted, however, that the plasma column alone exists if the source-plate edge is higher than 5 mm (leaving less than 41-mm gap between the source plate and the cavity ceiling). The stability of the titanium plasma-column is also presented by its microwave reflection. Its de-embedded reflection coefficient (with no impedance matching) remains stable during the 60-s run in the level of $|\Gamma| \sim 0.86$ with no significant phase changes.

Motions of plasma columns along the source-plate edge, from one corner to the other, have also been observed in most of the experimental runs. Figure 3 shows this back-and-forth motions by the time-varying positions of the plasma columns along the source-plate edge. The relative position, denoted as $x(t)$, is shown for five typical examples of plasma columns. The lateral speed of the titanium plasma-column motion observed along the source-plate edge may exceed ~1mm/s.

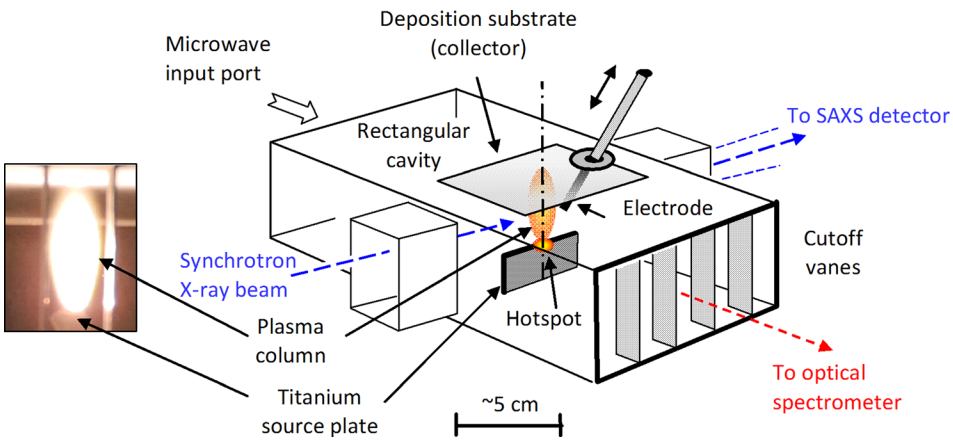

FIG. 1. The experimental setup of the 2.45-GHz microwave cavity[45] with a titanium electrode tilted at 50° with respect to the vertical axis. The vertical source plate is made of titanium.

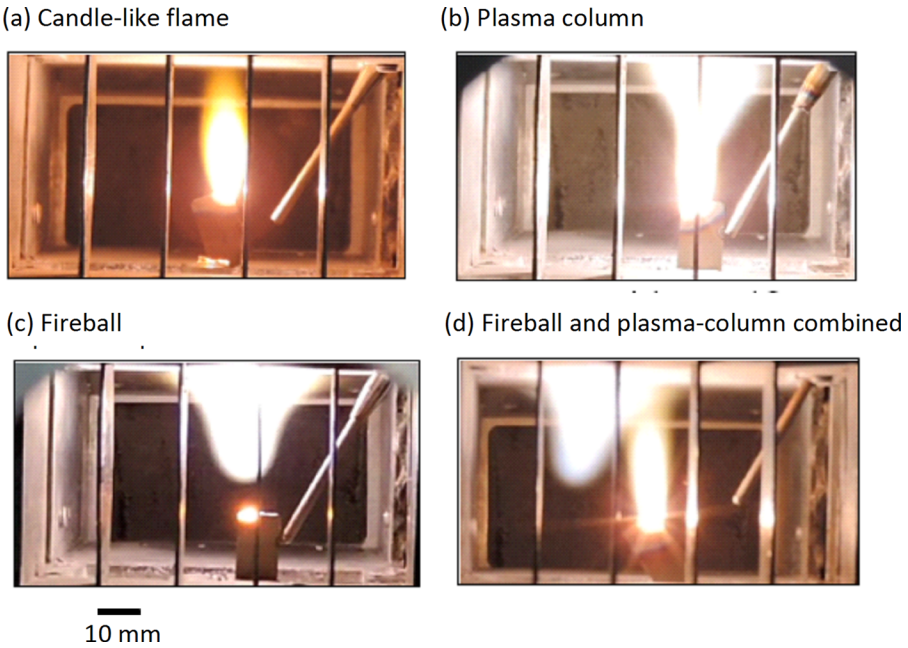

FIG. 2. Various shapes of plasma ejected from the titanium source in different runs within the microwave cavity: (a) initial evolution of the plasma column in a candle-flame shape, (b) an intense plasma column, (c) a fireball (plasmoid) detached from a hotspot on the source plate, and (d) a plasma column accompanied by a fireball.

The light emitted by the titanium plasma-column, as, for example, in Fig. 2(b), is recorded and analyzed by a calibrated optical spectrometer in the 200–1000 nm spectral range,[45] as shown in Fig. 4. The spectral lines near 445, 453, 482, 517, 590, and 592 nm are identified as titanium lines.[46,47] However, due to the 0.3-nm sampling resolution, some of these lines are overlapping or weak. The continuum radiation in the 420–440 and 580–620 nm ranges may also indicate the presence of titanium in the form of titanium nitride (TiN).[48–50] The 750–780 nm range reveals the titanium oxidation according to the γ-system band emission ($A^3\Phi - X^3\Delta$) from the TiO molecule.[49]

The titanium plasma-column was also investigated by SAXS.[51,52] The X-ray scattering at small-angles originates from spatial fluctuations of the electron density within the dusty plasma in the form of ionized nanoparticles. A quantitative analysis of SAXS from particulate systems provides the mean size, polydispersity, number density, and degree of aggregation of the particles.[51,52] The 2D SAXS pattern obtained from the plasma column is azimuthally averaged to yield the one-dimensional scattering curve shown in Section IV.

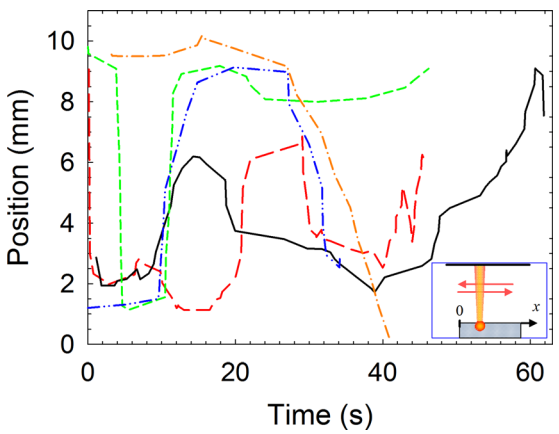

FIG. 3. The plasma-column motion along the edge of the source plate in five different experimental runs. The inset shows the coordinate x along the edge. The plasma column tends to move back and forth along the source-plate edge as seen in the typical examples in the graph.

B. *Ex-situ* observations

The experimental products of the titanium plasma-column, namely, both the eroded source plate and the deposited collector on the ceiling, were examined *ex-situ* by optical microscopy and by SEM in order to characterize their shape and composition. Figures 5(a) and 5(b) show optical microscopy images and Fig. 5(c) shows the analysis of a titania layer deposited on a copper substrate employed as a collector. (The image also shows the edge of the deposited layer in order to enable its thickness estimate.) This typical result shows a deposited layer of a ~55-μm mean thickness obtained in a 60-s period, which indicates a relatively high deposition rate (~1 μm/s in these conditions) compared to other plasma methods (e.g., Ref. 53 reviews various techniques of atmospheric plasma deposition, of which the highest deposition rate is ~0.1 μm/s). The uniformity of the deposit

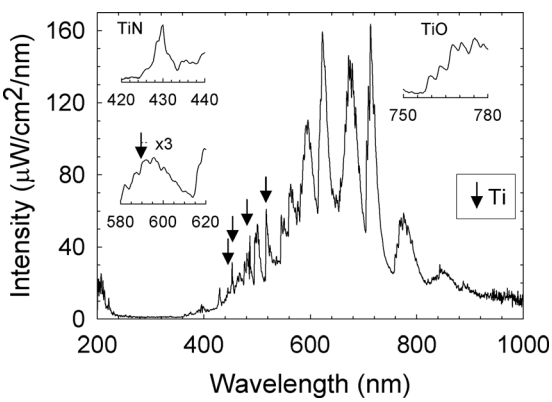

FIG. 4. Optical spectrum of the light emitted by the titanium plasma-column. The inset shows the presence of larger molecules such as titanium nitride and titanium oxide.

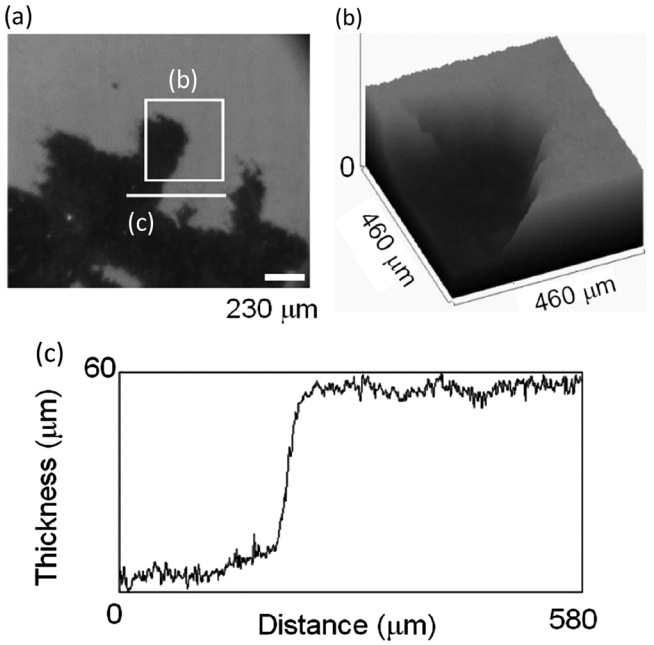

FIG. 5. A typical TiO_2 layer deposited on copper substrates during a 60-s period, profiled by an optical microscope image processing: (a) A 2D top view of the layer margin. (b) An enlarged 3D-image of the squared region marked in (a) above. (c) A 1-D cross-section profile of the deposited titania layer along the line marked in (a) above.

is estimated at ~4% (RMS) which is reasonably uniform (note that the uniformity depends here on various conditions which could be further improved).

SEM observations reveal particle morphologies and crystalline forms and show nanoparticles with various interconnected phases over areas of several square micrometers. Figures 6(a)–6(h) show titania morphologies obtained in different experimental runs with a vertical electrode, as observed by SEM on the deposited copper collectors and on the titanium source plate. The titania observed on the collector presents three types of crystalline morphologies, namely, elongated, hexagonal, and spherical, as seen in Figs. 6(a)–6(d), respectively. Those found on the source plate also display three types of morphologies, namely, hexagonal, elongated lamellar, and columns, as seen in Figs. 6(e)–6(h), respectively. Each of these forms shows a specific type of crystalline structure. Figures 6(a)–6(h) exhibit, respectively, structures of (a) interconnected star-like hexagonal and spherical crystalline particles; (b) hexagonal elongated particles arranged in long rows; (c) hexagonal particles deposited in a stratified form; (d) spherical type particles deposited in a rough spatial arrangement; (e) individual hexagonal crystalline particles with various spatial orientations; (f) partially interconnected hexagonal particles creating large plates in a preferred direction parallel to the deposition surface; (g) stratified lamellar plates growing from the surface; and (h) micrometer elongated needle-like columns of about 40-nm in diameter arranged parallel to each other along the surface. The titania particles sizes shown in Figs. 6(a)–6(h) can be divided into the ranges of 40–80 nm for small spherical particles and 80–150 nm for the hexagonal particles. The thickness of the elongated and column shaped particles is 30–50 nm.

Comparing the results shown in Figs. 6(a)–6(h) to data from the literature, one can identify the morphology in Fig. 6(a) as the rutile crystalline phase,[41] the ones in Figs. 6(b) and 6(c) as the brookite phase,[15,27,33] and in Fig. 6(d) as the anatase phase.[19,35–38,40] However, the phases observed on the source plate (Figs. 6(e)–6(h)) exhibit only the brookite and rutile phases, in Figs. 6(e) and 6(f) and Figs. 6(g) and 6(h), respectively. Thus, we assume that the particles observed in Figs. 6(b)–6(f) were obtained at temperatures lower than ~600 °C, and those shown in Figs. 6(a), 6(g), and 6(h) at temperatures higher than 600 °C. Since the rutile phase can be obtained by a thermal treatment of the brookite and anatase phases,[27–30] the titania morphology shown in

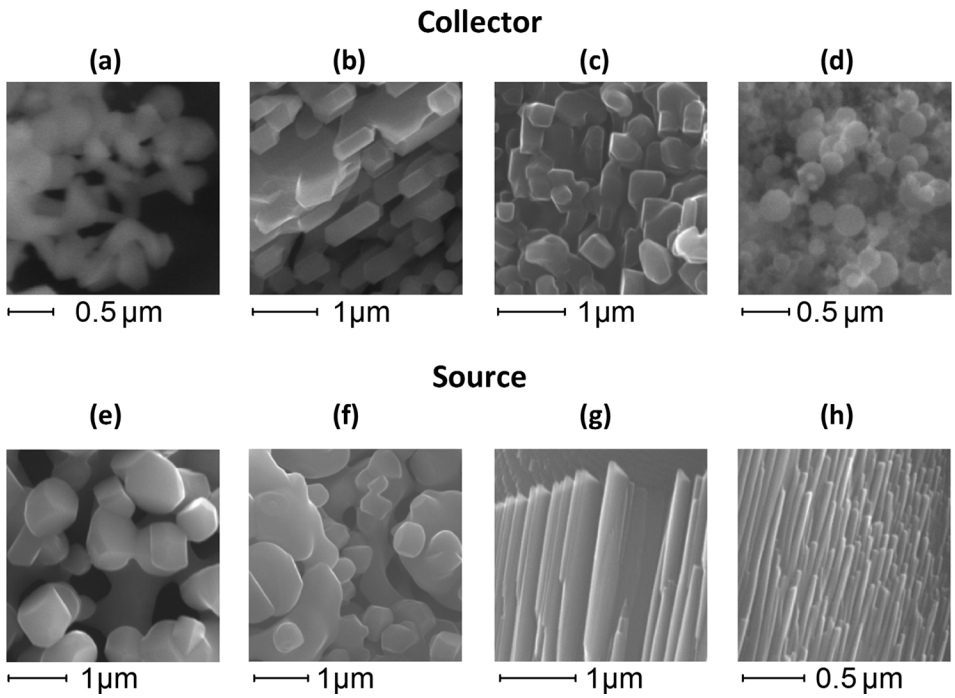

FIG. 6. Titania morphologies including rutile, brookite, and anatase phases observed by SEM on the copper collector ((a)–(d)) and on the titanium source plate ((e)–(h)) in different experimental runs. A vertical electrode was used in these experimental runs (rather than the tilted electrode shown in Fig. 1). The various morphologies observed are described in detail in the text.

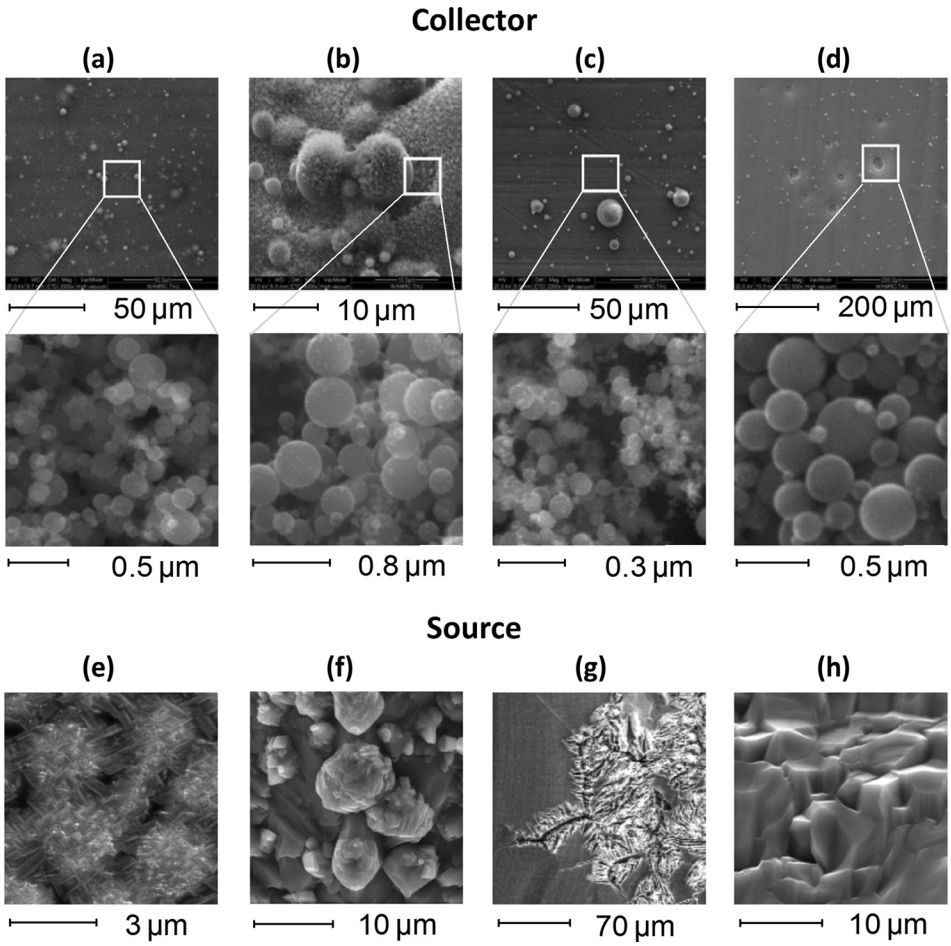

FIG. 7. Titania morphologies deposited on copper collectors of the anatase phase observed by SEM. A tilted electrode was used in these experimental runs for deposition periods of 40 and 60 s (in Figs. 7(a) and 7(b) and Figs. 7(c) and 7(d), respectively). Figures 7(e)–7(h) present SEM observations of the source plates corresponding to the collectors shown in Figs. 7(a)–7(d), respectively. The various morphologies observed are described in detail in the text.

Figs. 6(g) and 6(h) could possibly be formed at temperatures higher than ~600 °C, thus enabling the transformation of the brookite phase into rutile. The titania morphologies presented above are made possible due to the temporal and spatial variations in the plasma temperature, thus creating structural changes in the deposited powders and on the source plate.

SEM observations of titania depositions on copper collectors using a tilted electrode (as shown in Fig. 1) are presented in Figs. 7(a) and 7(b) and Figs. 7(c) and 7(d), for deposition periods of 40 and 60 s, respectively. Figures 7(e)–7(h) present SEM observations of the source plates corresponding to the collectors presented in Figs. 7(a)–7(d), respectively. Only the anatase phase is observed on the collector surface for the inclined electrode case. However, new morphological structures appear now on the source-plate surface. In the magnified Figs. 7(a)–7(d), the titania morphology show spherical nano-particles typical of the anatase phase. In Figs. 7(e) and 7(g), the morphology observed on the source surface is dendritic, whereas in Figs. 7(f) and 7(h) the morphology exhibits isolated particulate aggregates and extruded ones, respectively. The EDS analysis revealed Ti and O elements in all these samples.

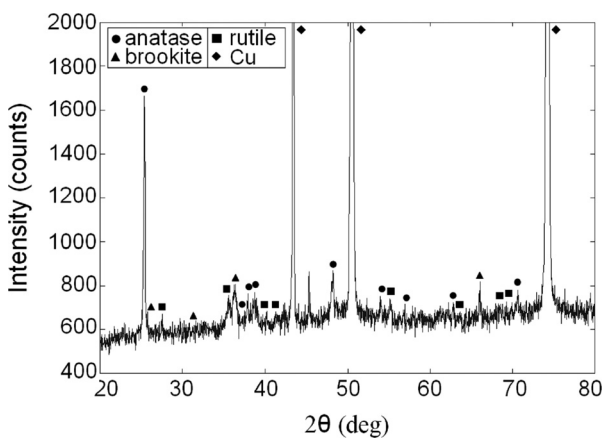

FIG. 8. An XRD diffraction pattern of a TiO_2 layer deposited in 60 s on a copper substrate.

The XRD analysis, presented in Fig. 8, of the titania deposited on copper collectors (with a tilted electrode) further supports the morphological analysis of its various phases. The anatase, brookite, and rutile crystalline phases of titania are identified. However, the most abundant crystalline form detected is the metastable anatase.

IV. ANALYSES

The identified spectral lines of titanium shown in Fig. 4 provide a measure of the plasma temperature. This can be estimated by using a Boltzmann plot of the line intensity, assuming a partial local thermal-equilibrium (pLTE) state of the plasma.[54] The intensity I_{ki} of the transition from the upper k to the lower i energy level is given in the Boltzmann equation

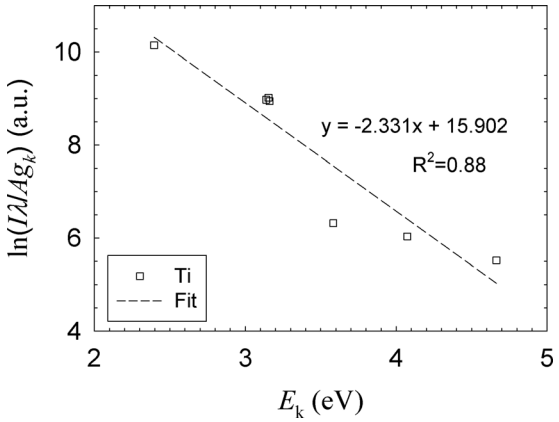

FIG. 9. Boltzmann plot applied to the titanium atomic lines detected in Fig. 4. The excitation temperature estimate results in ~0.4 eV.

$$\ln(I_{ki}\lambda_{ki}/g_k A_{ki}) = -(1/k_B T_{exc})E_k + \text{const.}, \quad (1)$$

where λ_{ki} and A_{ki} are the transition wavelength and probability, respectively, k_B is the Boltzmann constant, and E_k is the upper energy state with a g_k degeneracy. The excitation temperature is estimated by the slope of the graph presented in Fig. 9 as 0.4 eV(~4600 K). The relatively large scatter of the measurement results from the fit line is due to the 0.3-nm spectral resolution and the consequent overlap of the detected atomic lines (presented here with no deconvolution processing).

The average size distribution of the nanoparticles detected within the plasma column, their aggregation state, and surface-to-volume ratio is obtained by analyzing the azimuthally averaged 2D-SAXS normalized patterns.[51] Figure 10 shows results of the scattered X-ray intensity $I(Q)$ as a function of the modulus of the scattering vector $Q = (4\pi/\lambda)\sin(\theta/2)$, where λ is the wavelength of the incident X-ray radiation and θ is the scattering angle. The curve is modelled with the IRENA SAXS[52] analysis program using the unified scattering equation[51]

$$I(Q) = G\exp(-Q^2R_g^2/3) + B\{[\text{erf}(QR_g/\sqrt{6})]^3/Q\}^P, \quad (2)$$

where R_g is the radius of gyration, G is a pre-factor depending on the particle number and scattering length densities, B is a pre-factor depending on the average surface area of the particles, $\text{erf}(x)$ is the error function, and P is a power-law exponent. Thus, for compact objects with a sharp interface, $P = 4$ (whereas $3 \leq P \leq 4$ indicates the surface roughness of the particles characterized by a fractal dimension $F = 6 - P$).[51]

The values for the radius of gyration R_g, which depend on the G and P parameters,[52] are obtained using the unified fit of the scattered intensity $I(Q)$, as shown in Fig. 10 for two levels of the fit. In this example, for the small particles, the estimated value $R_{g1} = 28$ nm is obtained from the first level fit, whereas for the agglomerated particles it results in $R_{g2} = 285$ nm using the second level fit. The particles size distribution shown in Fig. 11 is obtained by the inverse Fourier transform of the scattered intensity $I(Q)$ using the IRENA-SAXS analysis program. Thus, for a typical titanium plasma-column, the size distribution of the particles is centered around ~40 nm.

The mean radius of gyration R_g is obtained from the unified fit evaluated by the IRENA SAXS program for 150 samples taken from 9 plasma columns observed. For the particles of titania plasma-columns, R_g varies from 48 nm for small particles to 275 nm for the agglomerated particles, with a standard deviation of 41% and 9.8%, respectively. From the size distribution analysis of about 130 samples obtained in the range of 10 to 500 s deposition period, the particles number density has a mean value of $d \sim 3.8 \times 10^{17}\,\text{m}^{-3}$ with standard deviation of ~36%, and the particles specific volume has a mean value of $V \sim 2.9 \times 10^{-7}$ with a standard deviation of 55%.

The SAXS results, combined with the microwave reflections measured at the input port of the cavity, enable us to estimate the effective electron density of the dusty plasma

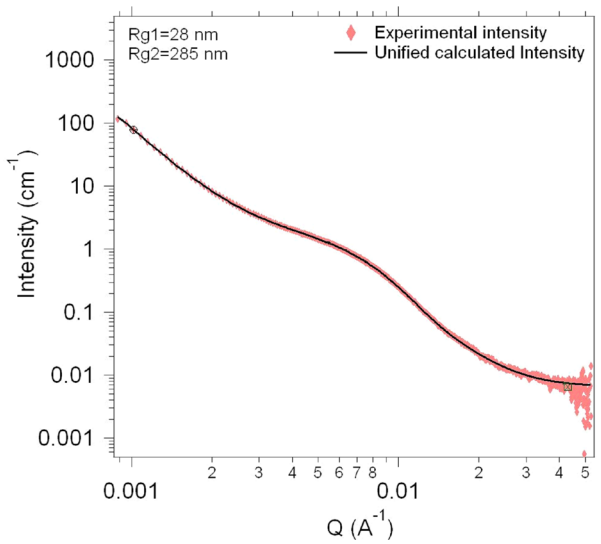

FIG. 10. The normalized SAXS intensity vs. the modulus of scattering vector Q for a typical titanium plasma-column, and its analysis using unified scattering function.

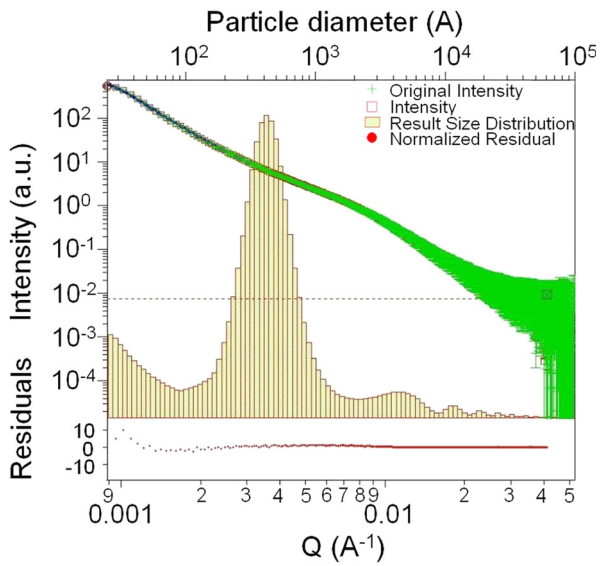

FIG. 11. Size distribution evaluation by SAXS for a typical titanium plasma-column.

evolved.[55] By fitting the simulation results to the measured reflections, the relative dielectric permittivity ε_r is found assuming a Gaussian radial distribution. The effective dielectric permittivity ε_r, consisting of the complex plasma permittivity $\varepsilon'_p - j\varepsilon''_p$ and of the dust conductivity σ_{ed}, is given by

$$\varepsilon_r = \varepsilon'_p - j\varepsilon''_p - j\sigma_{ed}/\varepsilon_0\omega, \tag{3}$$

where ε_0 is the vacuum permittivity and ω is the angular frequency. The dielectric permittivity of the plasma is given by its approximated real and imaginary components

$$\varepsilon'_p = 1 - \frac{\omega_p^2}{\omega^2 + \upsilon^2}, \tag{4a}$$

$$\varepsilon''_p = \frac{\omega_p^2 \upsilon}{\omega(\omega^2 + \upsilon^2)}, \tag{4b}$$

respectively, where $\omega_p = \sqrt{e^2 n_e/m_e\varepsilon_0}$ and υ are the plasma and the collision frequencies, respectively, and e, n_e, and m_e are the electron charge, density, and mass, respectively. The dusty plasma conductivity is given in similar conditions[55] as

$$\sigma_{ed} \cong \eta_{ed}\frac{\omega}{\hat{k}}\left[\frac{\omega^2 - \upsilon\upsilon_{ch}}{(\omega^2+\upsilon_{ch}^2)(\omega^2+\upsilon^2)} + j\omega\frac{\upsilon+\upsilon_{ch}}{(\omega^2+\upsilon_{ch}^2)(\omega^2+\upsilon^2)}\right], \tag{5}$$

where

$$\eta_{ed} = \omega_p^2\varepsilon_0/l_d \tag{6}$$

is the charging factor, $l_d = (n_d\pi r_d^2)^{-1}$ is the dust collision length factor, n_d and r_d are the dust grain density and the average particle radius, respectively, and $\hat{k}$ is the spatial angular frequency (the wave's wavenumber for a uniform plasma). The electron effective collision frequency is given by $\upsilon = V_{Te}\sigma_n N_n$, where $V_{Te} = \sqrt{k_B T_e/m_e}$ is the electron thermal velocity, σ_n and N_n are the neutrals cross-section and density, respectively, T_e is the electron temperature, and υ_{ch} is the dust charging frequency.

The simulation includes a microwave cavity as in Fig. 1 with a plasma column inside, represented by a dielectric cylinder of $h = 52$ mm height and $d_{PC} = 15$ mm diameter. The simulated Poynting vector and the power dissipation are shown in Fig. 12(a). In a more heuristic transmission-line model, illustrated in Fig. 12(b), the plasma column is represented by a lumped element having admittance $Y_{PC} = G_{PC} + jB_{PC}$ in a transmission line with a characteristic admittance Y_c of the waveguide TE_{10} mode ($Y_c = 2$ mS). The plasma column conductance and susceptance are approximated by $G_{PC} = \omega\varepsilon_0\varepsilon''_r A/h$ and $B_{PC} = \omega\varepsilon_0\varepsilon'_r A/h$, respectively, where A is the effective plasma-column cross-section area. In this analysis (as in Ref. 54), the complex ε_r space is scanned numerically by the electromagnetic (EM) simulation in order to find the conditions that provide the reflections measured in the experiments. The real part of ε_r is initially chosen as 0.2, while the imaginary part is searched between 3 and 1000. The simulated results and the experimental observations are presented in the Smith chart in Fig. 13. The simulated results give an estimate for the effective dissipation factor (including conductivity) as $\varepsilon''_r \sim 300$, where the average experimental reflection is 0.89. This value yields reflection coefficient of 0.88 according to the heuristic 1D model shown in Fig. 12(b). Using the ~0.4 eV excitation temperature found by Boltzmann plot and the dust particle size obtained by SAXS analyses above, the corresponding electron density in this case is estimated by

$$n_e \sim \frac{m_e\varepsilon_0\varepsilon''_r}{e^2}\frac{\omega^2+\upsilon^2}{\upsilon/\omega + 1/\hat{k}l_d}, \tag{7}$$

where $\hat{k}$ is approximated by $\sim\pi/d_{PC}$ for the finite transverse profile of the plasma column. Equation (7) yields

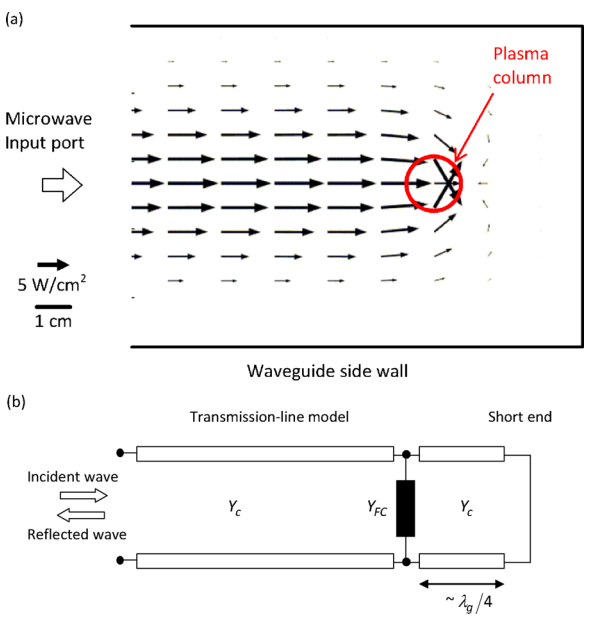

FIG. 12. (a) A numerical simulation of the Poynting vector power-flow across the horizontal plane of the plasma column in the cavity for the parameters listed in Table I. (b) An analytical transmission-line model of the reflection from the plasma-column as a lumped element.

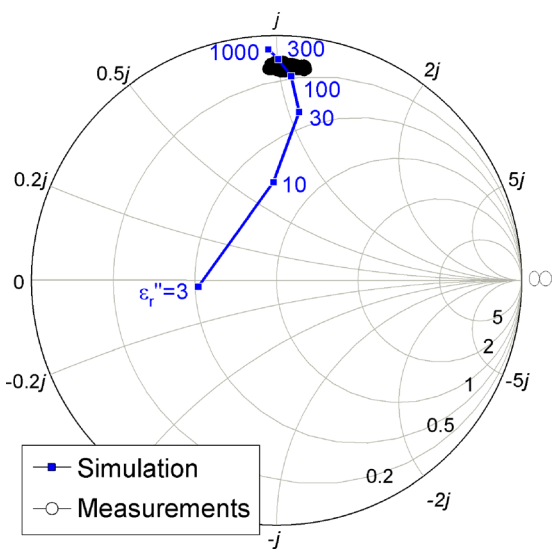

FIG. 13. A Smith-chart presentation of the plasma column reflectivity Γ (modulus and phase) during TiO_2 deposition on copper for 45 s. The experimental value (open circles) accumulated in >2000 samples fit the blue track of the simulated plasma column of $d_{PC} = 15$ mm diameter for $\varepsilon''_r \sim 300$.

$n_e \sim 10^{19}$ m^{-3}, similarly to other plasma forms at atmospheric pressure in air.[56,57]

V. DISCUSSION

This work investigated the titanium plasma-column generated by localized microwaves at atmospheric pressure and its products observed as titania nano-powder deposited on copper substrates. The plasma column is created by a titanium electrode brought into contact with a titanium plate while irradiated by microwaves at 2.45 GHz generated by a ~1-kW magnetron.

In experiments conducted with a vertical electrode, the plasma columns lasted for more than a minute and deposited titania nano-powder on copper in various crystalline forms at high rate of ~1 μm/s. Experiments conducted with a tilted electrode configuration yielded a more uniform deposition of mainly anatase phase in deposition periods of 40–60 s. The better uniformity obtained by the tilted electrode is attributed to the more homogeneous unobstructed plasma column in this case. The deposition speed of ~1 μm/s achieved in these experiments is about 10-times faster than reported for conventional plasma deposition in atmospheric pressure.[53]

For the analysis of the dusty plasma column, the SAXS measurements provide information about the size distribution and density of the nano-particles. The distributed particle size has a peak centered around ~40 nm and a typical mean density of $\sim 3.8 \times 10^{17}$m^{-3}. SEM observations revealed the structure and morphology of the deposited particles, which consist mainly of the anatase phase. Some rutile and hexagonal brookite phases have also been identified. The existence of these phases is confirmed by XRD observations, showing predominantly the anatase crystalline phase. The SEM observations also show typical morphologies of titania in various aggregated forms, e.g., lamellar plates, elongated columns, and networks of particles.

In view of the possibility of obtaining a variety of crystalline polymorphs of titania in various spatial arrangements, this technique can be considered for the production of titania deposits on various substrates of interest, for applications involving nanometric crystals.

The microwave plasma-column technique can be sustained in an ambient atmosphere at room temperature; hence, it may provide a practical tool for a variety of applications. The titania plasma column generated by localized microwaves in air atmosphere may also be used for metallurgical applications, such as metal treatments for surface hardening. In other applications, the collector substrates, onto which titanium dioxide is deposited, can be used, for example, in photo-catalytic devices[9–14] due to the pertinent titania properties.

The microwave plasma-column technique[43] shows potential advantages of controllability and uniformity by a direct and fast deposition of titania. This technique allows thin films to be deposited rapidly at room temperature, in air atmosphere. The low power consumption involved makes it inexpensive, and the nanoparticles can be formed directly from the metal substrate without the need for chemical precursors. As compared to other techniques[31–41] mentioned above, one can conclude that the microwave plasma-column technique provides the required anatase crystalline layer directly with a homogeneous morphology on the substrate in a single step without further heat or annealing treatments. Further studies may aim at the selective synthesis of one particular polymorph with the required crystalline phase (e.g., anatase) on the substrate. It is envisaged that using this technique to deposit titania on glass and similar substrates could be beneficial for applications such as titania based solar-cells and oxygen sensors.

ACKNOWLEDGMENTS

This study was supported by the Israel Science Foundation (ISF) Grant No. 1639/11. The authors also acknowledge Dr. Michael Sztucki for his help with the synchrotron experiment, ESRF for synchrotron beam time, and Mr. Sheferaw Wonde for his technical assistance at TAU.

[1]A. Khataee and G. A. Mansoori, *Nanostructured Titanium Dioxide Materials: Properties, Preparation and Applications* (World Scientific Publishing Company, Singapore, 2011).
[2]M. Pelaez, N. Nolan, S. Pillai, M. K. Seery, P. Falaras, A. G. Kontos, P. S. M. Dunlop, J. W. J. Hamiltone, J. A. Byrne, K. O'Shea, M. H. Entezari, and D. D. Dionysiou, "A review on the visible light active titanium dioxide photo-catalysts for environmental applications," Appl. Catal., B **125**, 331 (2012).
[3]A. Sobczyk-Guzenda, H. Szymanowski, W. Jakubowski, A. Błasinska, J. Kowalski, and M. Gazicki-Lipman, "Morphology, photo-cleaning and water wetting properties of cotton fabrics, modified with titanium dioxide coatings synthesized with plasma enhanced chemical vapor deposition technique," Surf. Coat. Technol. **217**, 51 (2013).
[4]T. Baran and W. Macyk, "Photo-catalytic oxidation of volatile pollutants of air driven by visible light," J. Photochem. Photobiol., A **241**, 8 (2012).
[5]G. E. Romanos, C. P. Athanasekou, F. K. Katsaros, N. K. Kanellopoulos, D. D. Dionysiou, V. Likodimos, and P. Falaras, "Double-side active TiO_2-modified nano-filtration membranes in continuous flow photo-catalytic reactors for effective water purification," J. Hazard. Mater. **211–212**, 304 (2012).
[6]T. Ochiai, K. Masuko, S. Tago, R. Nakano, Y. Niitsu, G. Kobayashi, K. Horio, K. Nakata, T. Murakami, M. Hara, Y. Nojima, M. Kurano, I. Serizawa, T. Suzuki, M. Ikekita, Y. Morito, and A. Fujishima, "Development of a hybrid environmental purification unit by using of excimer VUV lamps with TiO_2 coated titanium mesh filter," Chem. Eng. J. **218**, 327 (2013).
[7]C. Ying, W. Cuifang, B. Bo, and Y. Li, "Fabrication of TiO_2 hollow spheres using yeast as bio-templates and their photo-catalytic performance for the degradation of CBW wastewater," in 4th Int'l Conf. on Bioinformatics & Biomedical Engineering (iCBBE), Chengdu, 18–20 June 2010.
[8]Y. Nakamura, F. Kobayashi, M. Daidai, and A. Kurosumi, "Purification of seawater contaminated with un-degradable aromatic ring compounds using ozonolysis followed by titanium dioxide treatment," Mar. Pollut. Bull. **57**, 53 (2008).
[9]M. Hunger, G. Husken, and H. J. H. Brouwers, "Photo-catalytic degradation of air pollutants: From modeling to large scale application," Cem. Concr. Res. **40**, 313 (2010).
[10]A. Kleiman, A. Marquez, M. L. Vera, J. M. Meichtry, and M. I. Litter, "Photo-catalytic activity of TiO_2 thin films deposited by cathodic arc," Appl. Catal., B **101**, 676 (2011).
[11]H. S. Mazloomi Tabaei, M. Kazemeini, and M. Fattahi, "Preparation and characterization of visible light sensitive nano titanium dioxide photo-catalyst," Sci. Iran., Trans. C **19**, 1626 (2012).
[12]Y. Ono, T. Rachi, M. Yokouchi, Y. Kamimoto, A. Nakajima, and K. Okada, "Photo-oxidation of gaseous ethanol on photo-catalyst prepared by acid leaching of titanium oxide/hydroxyapatite composite," Mater. Res. Bull. **48**, 2272 (2013).

[13]K. Govindan, S. Murugesan, and P. Maruthamuthu, "Photo-catalytic degradation of pentachlorophenol in aqueous solution by visible light sensitive N-F-codoped TiO_2 photocatalyst," Mater. Res. Bull. **48**, 1913 (2013).
[14]M. Tazawa, M. Okada, K. Yoshimura, and S. Ikezawa, "Photo-catalytic heat mirror with a thick titanium dioxide layer," Sol. Energy Mater. Sol. Cells **84**, 159 (2004).
[15]N. Duraisamy, N. Malik Muhammad, H. C. Kim, J. D. Jo, and K. H. Choi, "Fabrication of TiO2 thin film memristor device using electro-hydrodynamic inkjet printing," Thin Solid Films **520**, 5070 (2012).
[16]K. F. Albertin and I. Pereyra, "Study of reactive sputtering titanium oxide for metal-oxide-semiconductor capacitors," Thin Solid Films **517**, 4548 (2009).
[17]W. Weppner, "Oxide semiconductors for solar energy conversion-titanium dioxide," Int. J. Hydrogen Energy **37**, 4535 (2012).
[18]J. Nowotny, T. Bak, M. K. Nowotny, and L. R. Sheppard, "Titanium dioxide for solar-hydrogen I. Functional properties," Int. J. Hydrogen Energy **32**, 2609 (2007).
[19]S. Middlemas, Z. Zak Fang, and P. Fan, "A new method for production of titanium dioxide pigment," Hydrometallurgy **131–132**, 107 (2013).
[20]S. Wijewardane and D. Y. Goswami, "A review on surface control of thermal radiation by paints and coatings for new energy applications," Renewable Sustainable Energy Rev. **16**, 1863 (2012).
[21]D. R. Tennant, "Screening potential intakes of color additives used in non-alcoholic beverages," Food Chem. Toxicol. **46**, 1985 (2008).
[22]M. D. Newman, M. Stotland, and J. I. Ellis, "The safety of nano-sized particles in titanium dioxide and zinc oxide based sunscreens," J. Am. Acad. Dermatol. **61**, 685 (2009).
[23]J. Schulz, H. Hohenberg, F. Pflücker, E. Gärtner, T. Will, S. Pfeiffer, R. Wepf, V. Wendel, H. Gers-Barlag, and K. P. Wittern, "Distribution of sunscreens on skin," Adv. Drug Delivery Rev. **54**, S157 (2002).
[24]V. Stengl, S. Bakardjieva, N. Murafa, J. Subrt, H. Meatankova, and J. Jirkovsky, "Preparation, characterization and photocatalytic activity of optically transparent titanium dioxide particles," Mater. Chem. Phys. **105**, 38 (2007).
[25]S. Tosoni, O. Lamiel-Garcia, D. F. Hevia, J. M. Dona, and F. Illas, "Electronic structure of f-doped bulk rutile, anatase, and brookite polymorphs of TiO2," J. Phys. Chem. C **116**, 12738 (2012).
[26]M. Landmann, E. Rauls, and W. G. Schmidt, "The electronic structure and optical response of rutile, anatase and brookite TiO_2," J. Phys.: Condens. Matter **24**, 195503 (2012).
[27]J. G. Li and T. Ishigaki, "Brookite → rutile phase transformation of TiO_2 studied with monodispersed particles," Acta Mater. **52**, 5143 (2004).
[28]J. Huberty and H. Xu, "Kinetics study on phase transformation from titania polymorph brookite to rutile," J. Solid State Chem. **181**, 508 (2008).
[29]F. M. Hossain, L. Sheppard, J. Nowotny, and G. E. Murch, "Optical properties of anatase and rutile titanium dioxide – *Ab initio* calculations for pure and anion-doped material," J. Phys. Chem. Solids **69**, 1820 (2008).
[30]Q. Gao, X. Wu, and Y. Fan, "The effect of iron ions on the anatase–rutile phase transformation of titania (TiO_2) in mica–titania pigments," Dyes Pigm. **95**, 96 (2012).
[31]P. Angerer, L. G. Yu, K. A. Khor, and G. Krumpel, "Spark-plasma-sintering (SPS) of nanostructured and submicron titanium oxide powders," Mater. Sci. Eng., A **381**, 16 (2004).
[32]D. Handtrack, F. Despang, C. Sauer, B. Kieback, N. Reinfried, and Y. Grin, "Fabrication of ultra-fine grained and dispersion-strengthened titanium materials by spark plasma sintering," Mater. Sci. Eng., A **437**, 423 (2006).
[33]K. Vijayalakshmi, S. D. Jereil, and K. Karthick, "Effect of pyrolytic temperature on the properties of TiO2/ITO films for hydrogen sensing," Spectrochim. Acta, Part A **138**, 241 (2015).
[34]Y. C. Hong and H. S. Uhm, "Production of nano-crystalline TiO_2 powder by a microwave plasma-torch and its characterization," Jpn. J. Appl. Phys., Part 1 **46**, 6027 (2007).
[35]Y. C. Hong, T. Lho, B. J. Lee, H. S. Uhm, O.-P. Kwon, and S. H. Lee, "Synthesis of titanium dioxide in $O_2/Ar/SO_2/TiC_{l4}$ microwave torch plasma and its band gap narrowing," Curr. Appl. Phys. **11**, 517 (2011).
[36]A. Kleiman, A. Marquez, and D. G. Lamas, "Anatase TiO_2 films obtained by cathodic arc deposition," Surf. Coat. Technol. **201**, 6358 (2007).
[37]M. Shigeta and A. B. Murphy, "Thermal plasmas for nanofabrication," J. Phys. D: Appl. Phys. **44**, 174025 (2011).
[38]F. Fang, J. Kennedy, E. Manikandan, J. Futter, and A. Markwitz, "Morphology and characterization of TiO2 nano-particles synthesized by arc discharge," Chem. Phys. Lett. **521**, 86 (2012).
[39]T. Peng, D. Zhao, K. Dai, W. Shi, and K. Hirao, "Synthesis of titanium dioxide nanoparticles with mesoporous anatase wall and high photocatalytic activity," J. Phys. Chem. B **109**, 4947 (2005).
[40]J.-W. Kim, J.-W. Kim, J.-W. Shim, J.-H. Bae, S.-H. Han, H.-K. Kim, I.-S. Chang, H.-H. Kang, and K.-D. Suh, "Titanium dioxide polymethyl methacrylate composites microspheres prepared by *in situ* suspension polymerization and their ability to protect against UV rays," Colloid Polym. Sci. **280**, 584 (2002).
[41]Y. Li and G. P. Demopoulos, "Precipitation of nanosized titanium dioxide from aqueous titanium (IV) chloride solutions by neutralization with MgO," Hydrometallurgy **90**, 26 (2008).
[42]M. Koelsch, S. Cassaignon, C. T. T. Minh, J. F. Guillemoles, and J. P. Jolivet, "Electrochemical comparative study of titania (anatase, brookite and rutile) nanoparticles synthesized in aqueous medium," Thin Solid Films **451–452**, 86 (2004).
[43]E. Jerby, A. Golts, Y. Shamir, S. Wonde, J. B. A. Mitchell, J. L. LeGarrec, T. Narayanan, M. Sztucki, D. Ashkenazi, Z. Barkay, and N. Eliaz, "Nanoparticle plasma ejected directly from solid copper by localized microwaves," Appl. Phys. Lett. **95**, 191501 (2009).
[44]V. Dikhtyar and E. Jerby, "Fireball ejection from a molten hot-spot to air by localized microwaves," Phys. Rev. Lett. **96**, 045002 (2006).
[45]Y. Meir and E. Jerby, "Breakdown spectroscopy induced by localized microwaves for material identification," Microwave Opt. Technol. Lett. **53**, 2281 (2011).
[46]H. R. Griem, *Plasma Spectroscopy* (McGraw-Hill, New York, 1964).
[47]A. Kramida, Yu. Ralchenko, J. Reader, and NIST ASD Team (2014), NIST Atomic Spectra Database (Ver. 5.2), National Institute of Standards and Technology, Gaithersburg, MD, available online http://physics.nist.gov/asd [last accessed December 22, 2014].
[48]E. Restrepo and A. Devia, "Optical emission diagnostic of a pulsed arc discharge," J. Vac. Sci. Technol., A **22**, 377 (2004).
[49]A. D. Giacomo, M. Dell'Aglio, A. Santagata, and R. Teghil, "Early stage emission spectroscopy study of metallic titanium plasma induced in air by femtosecond and nanosecond laser pulses," Spectrochim. Acta, Part B **60**, 935 (2005).
[50]A. R. Nassar, R. Akarapu, S. M. Copley, and J. A. Todd, "Investigations of laser-sustained plasma and its role in laser nitriding of titanium," J. Phys. D: Appl. Phys. **45**, 185401 (2012).
[51]G. Beaucage, "Approximations leading to a unified exponential power-law approach to small-angle scattering," J. Appl. Crystallogr. **28**, 717 (1995).
[52]J. Ilavsky and P. R. Jemian, "Irena: Tool suite for modeling and analysis of small-angle scattering," J. Appl. Crystallogr. **42**, 347 (2009).
[53]D. Merche, N. Vandencasteele, and F. Reniers, "Atmospheric plasmas for thin film deposition: A critical review," Thin Solid Films **520**, 4219 (2012).
[54]Y. Meir, E. Jerby, Z. Barkay, D. Ashkenazi, J. B. A. Mitchell, T. Narayanan, N. Eliaz, J. L. LeGarrec, M. Sztucki, and O. Meshcheryakov, "Observations of ball-lightning-like plasmoids ejected from silicon by localized microwaves," Materials **6**, 4011 (2013).
[55]Y.-X. Shi, D.-B. Ge, and J. Wu, "Theoretical analysis of microwave attenuation constant of weakly ionized dusty plasma," Chin. J. Geophys. **50**, 877 (2007).
[56]J. Park, I. Henins, H. W. Herrmann, G. S. Selwyn, J. Y. Jeong, R. F. Hicks, D. Shim, and C. S. Chang, "An atmospheric pressure plasma source," Appl. Phys. Lett. **76**, 288 (2000).
[57]X. Lu, M. Laroussi, and V. Puech, "On atmospheric-pressure non-equilibrium plasma jets and plasma bullets," Plasma Sources Sci. Technol. **21**, 034005 (2012).